



Evolution of Crack Source Mechanisms in Laboratory Hydraulic Fracturing on Harcourt Granite

Xin Zhang¹ · Guangyao Si¹ · Jung Oh¹ · Guozhen Zhao²

Received: 20 January 2024 / Accepted: 7 May 2024
© The Author(s) 2024

Abstract

Hydraulic fracturing has gained escalating significance in recovering unconventional reservoirs. However, the failure mechanism and its evolution with progressive fluid injection are not fully understood for granitic materials. To investigate, triaxial hydraulic fracturing on Harcourt granite and acoustic emission (AE) monitoring was performed by the self-developed multi-physical rock testing platform (MRTP). Source mechanism analysis suggests that tensile cracks account for the majority (62%) of all cracks throughout the hydraulic fracturing process. Tensile cracks with large energy are induced mainly around the borehole bottom, but their average energy is smaller than shear cracks. The entire hydraulic fracturing process is divided into three stages by injection measurements. In Stage 1, AE events are recorded with low energy emissions but high signal-to-noise ratios, revealing the initiation of hydraulic fractures before peak injection pressure. Tensile cracks are more dominant (78%) than other stages. In Stage 2, the number and magnitude of AE events increase exponentially along the trace formed in Stage 1. In Stage 3, hydraulic fractures have the largest magnitude among all stages. Shear cracks are nearly the same proportion as Stage 2, but more shear cracks with large magnitudes are observed following the trace formed by tensile cracks. A dense population of shear cracks can be found at the borehole bottom, and their distribution follows the average slip plunge of individual shear cracks induced by the injection fluid.

Highlights

- Mapping the spatial and temporal distribution of different source mechanisms induced by tri-axial hydraulic fracturing on Harcourt granite.
- Tensile cracks possess a much greater proportion than shear cracks among all hydraulic fractures.
- The proportion of tensile cracks during the initiation of hydraulic fractures is much larger than that in other periods.
- Majority of high-energy shear cracks are induced after the occurrence of massive tensile cracks.
- The trace of shear cracks follows the average slip plunge of individual shear cracks.

Keywords Tri-axial hydraulic fracturing · Unconventional reservoirs · Acoustic emission · Source mechanism · Harcourt granite

✉ Guangyao Si
g.si@unsw.edu.au

¹ School of Minerals and Energy Resources Engineering, University of New South Wales, Sydney, NSW 2052, Australia

² College of Mining Engineering, Taiyuan University of Technology, Taiyuan 030024, Shanxi, China

1 Introduction

Hydraulic fracturing has emerged as a dominant approach to generate extensive fractures or connected fracture networks. Apart from tectonic stress measurement (Fairhurst 1964) and rock formation preconditioning (He et al. 2016), it has proven effective for stimulation purposes both in conventional and unconventional oil/gas reservoirs (Temizel et al. 2022). Recently, it has been used overwhelmingly to extract shale gas of large depths, harvest thermal energy in

enhanced geothermal systems (EGS), and sequester carbon dioxide in deep rock formations (Fu et al. 2017). Of particular interest is the application in hot dry rock (HDR) formations, a promising source of heat energy. HDR formations, predominantly composed of hard rocks like granites, exhibit naturally low permeability due to their igneous origin and coarse-grained structure, distinguishing them from the sedimentary formations typically found in oil or gas reservoirs (Kumari et al. 2018).

Despite numerous hydraulic fracturing treatments conducted in various industries under different operational schemes and in situ conditions, the rock failure mechanism under fluid injection is not fully understood. The conventional fracturing theories offer clear and fundamental interpretations (Economides and Nolte 2000), but their assumptions fall short of encompassing all the conditions given the growing geological complexity encountered in practice. Rather than exhibiting a uniform percentage of purely tensile or shear crack modes under pressurized injection fluid, most failures display hybrid or mixed source mechanisms, especially for complex geological systems in unconventional reservoirs (Fischer and Guest 2011). Rock shearing failures are believed usually to happen within pre-existing fractures or faults under fluid injection. However, an increased prevalence of shear cracks has been observed within the intact matrix of coarse-grained rocks, such as crystalline granites, which has been substantiated through microscopic imaging (Zhuang and Zang 2021). More work has been attracted by understanding the shearing effect on rocks in relation to not only large faults or bedding planes but also micro-scale defects in intact materials (Ishida, et al. 2000; Rathnaweera et al. 2020; Zhuang et al. 2022). Nevertheless, the spatial distribution and temporal evolution of these newly found shear cracks have not been well characterized. Factors affecting the occurrence of shear cracks and their relationships with other crack modes have not been fully investigated.

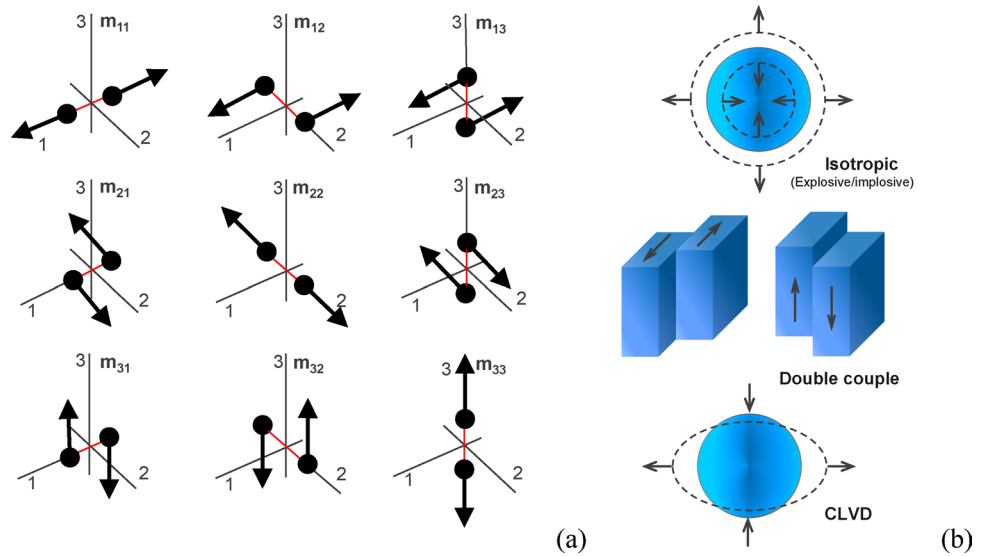
Induced seismicity is a significant outcome resulting from rocks' failure in hydraulic fracturing. Characterising the failure process and its mechanism by seismic analysis would not only enhance the efficiency of ongoing hydraulic fracturing operations but also aid in mitigating the damage caused by injection-induced earthquakes (Schultz et al. 2020). Field in situ study is typically project based and varies between cases due to unique geological conditions at each site. It typically faces numerous challenges, such as the elevated expenses associated with equipment set-up and test coordination, inadequately designed sensor networks, suboptimal signal acquisition, unexpected interference from human or natural activities, and limitations in data processing and interpretation (Grigoli et al. 2017; Wang et al. 2021). Alternatively, lab experiments

also play a critical role in testing natural rocks and examining the associated seismic effect both in isotropic and layered specimens (Lockner 1993; Goodfellow et al. 2013; Li et al. 2022, 2023). It can facilitate a better understanding of the initiation and propagation of hydraulic fractures and provide design improvements to field operations. Results from lab-scale tests can also contribute to the calibration of numerical and theoretical research to study large-scale models, thereby benefiting field applications (Zhang et al. 2023). In addition to the conventional analysis of AE source location and waveform characterization, advanced seismic analysis such as source mechanism inversion has been developed for lab data interpretation.

For instance, active and passive seismic monitoring was combined to map the evolution of hydraulic fractures' initiation and propagation in low-permeability sandstone (Stanchits et al. 2014) and tight granitic rocks (Butt et al. 2023a). Gehne et al. (2019) conceptualized two models to interpret diverse fracture propagations in sedimentary rocks by correlating distinct seismic responses, injection pressure variation, and induced deformation. Another set of hydraulic fracturing tests was performed on granite to investigate the displacement of different failure modes and their contribution to the volumetric deformation (Hampton et al. 2018). More recently, hydraulic fracturing tests have been conducted under various fracture propagation regimes. Higher viscosity of injection fluid was found to cause more dominance of tensile cracks brought by the fracture initiation (Butt et al. 2023b). However, more investigations need to be dedicated to confirm if viscosity is the only impact factor on this dominance. The effects from other parameters such as sample dimensions or injection rates are yet to be explored.

These previous investigations have made significant contributions to better understanding rock's failure process, but there is still a gap in discerning the evolution of distinct source mechanisms during the dynamic injection process. The dominance of different cracking modes over the initiation and propagation of hydraulic fractures remains largely unknown. The investigation into characterizing shear cracks in rock samples dominated by hydraulic fracturing-induced tensile cracks has been rarely reported. In this research, tri-axial hydraulic fracturing experiments with low-viscosity fluid are performed on Harcourt granite. Besides recording radiated seismic waveforms and induced deformation, the research aims to examine different failure modes and their variation in proportion and energy throughout the entire rock failure process. Simultaneously, AE event distribution with different source mechanisms in Harcourt granite is analyzed separately, expecting to establish their spatial and temporal

Fig. 1 Conceptual diagram of a seismic moment tensor: **a** Nine components of a moment tensor matrix; **b** Three decomposed components from the moment tensor



relationships, as well as their impact on hydraulic fractures’ initiation and ultimate geometry.

2 Theories of Source Mechanism Analysis

2.1 Inversion Fundamentals

The elastic wave radiated from a crack can be simulated when the force is loaded onto a point in an elastic material. A double couple of equivalent point forces are required to describe the force-driven faulting (Aki and Richards 1980). In the Cartesian coordinate system, 9 different force couples seen in Fig. 1a construct the moment tensor matrix:

$$\mathbf{M} = \begin{bmatrix} m_{11} & m_{12} & m_{13} \\ m_{21} & m_{22} & m_{23} \\ m_{31} & m_{32} & m_{33} \end{bmatrix}. \tag{1}$$

The moment tensor matrix describes the deformation at a source based on created force couples. Since the force couples can be calculated from symmetric stress tensor, the matrix is symmetric with only six independent elements (i.e., $m_{12} = m_{21}$). Thereafter, the seismic source can be represented by a seismic moment tensor, which is a 3 by 3 symmetric matrix of the detected crack failure and can be calculated by this equation (Aki and Richards 1980):

$$\mathbf{d} = \mathbf{G}\mathbf{m}, \tag{2}$$

where \mathbf{d} is the observed seismic waveforms in terms of displacement vector. In this model, elementary amplitude in the vector \mathbf{d} is corrected for ray paths and sensor effects considering the sensor’s polarity, geometrical distribution and coupling effect with the sample. \mathbf{G} is the Green’s function and

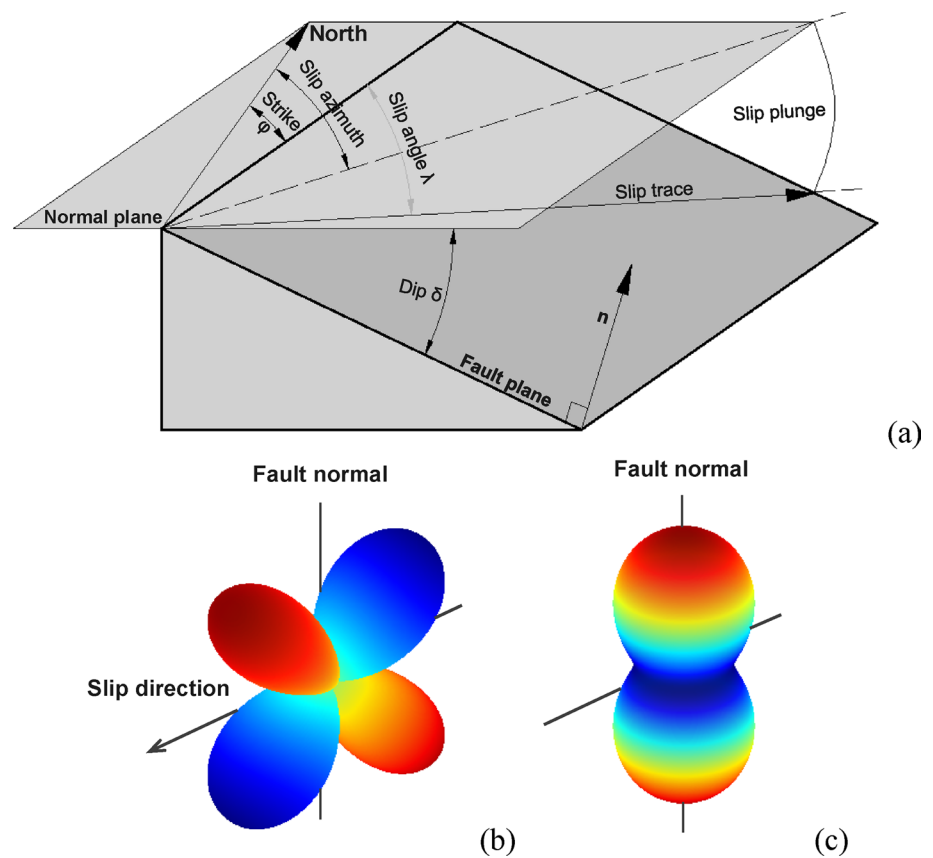
\mathbf{m} is the target moment tensor with six independent components. For one seismic source, Eq. (2) can be expressed as follows to become discretized:

$$\begin{bmatrix} u_1 \\ u_2 \\ \vdots \\ u_k \end{bmatrix} = \begin{bmatrix} G_{1,11} & G_{1,12} & \dots & G_{1,33} \\ G_{2,11} & G_{2,22} & \dots & G_{2,33} \\ \vdots & \vdots & \vdots & \vdots \\ G_{k,11} & G_{k,22} & \dots & G_{k,33} \end{bmatrix} \begin{bmatrix} m_{11} \\ m_{12} \\ m_{13} \\ m_{22} \\ m_{23} \\ m_{33} \end{bmatrix} \tag{3}$$

The left side of Eq. (3) represents k sets of recorded seismic data from sensor No.1 to sensor No. k . Every row of the \mathbf{G} matrix on the right side represents a vector of Green’s functions for every individual sensor. The key step is to obtain the desirable Green’s function (\mathbf{G}) that describes the radiation pattern of the source (Fig. 2b and c) and the nature of wave traveling mediums affecting the waveform generation (De Natale and Zollo 1989). Specifically, the radiation pattern depicts the variation of wave amplitude with directions in a source. A common practice for acquiring the Green’s function is to consider the P-wave’s first motion polarity with the first arrival and amplitudes (Stump and Johnson 1977; Ohtsu 1995). Assuming the homogeneity and isotropy of the material, the recorded waveform of individual sensor k on the left side of Eq. (3) can be extended as follows to obtain one group of five elements on the right side of Eq. (3):

$$\text{Amp}_k = C_k \frac{\text{Ref}(t, r)}{R_k} \begin{bmatrix} r_1 \\ r_2 \\ r_3 \end{bmatrix}^T \cdot \begin{bmatrix} m_{11} & m_{12} & m_{13} \\ m_{21} & m_{22} & m_{23} \\ m_{31} & m_{32} & m_{33} \end{bmatrix} \cdot \begin{bmatrix} r_1 \\ r_2 \\ r_3 \end{bmatrix} \tag{4}$$

Fig. 2 **a** Schematic geometry of a fault plane (after Stein and Wyession 2003) and the radiation patterns of fault plane solutions: **b** Pure shear source of P-wave; **c** Pure tensile source of P-wave



where Amp_k is the first motion amplitude of the original waveform recorded by sensor k .

C_k is the calibration coefficient depending on the sensor sensitivity and material constant. In this experiment,

$C_k=1$ since all the sensors are equally well calibrated.

R_k is the ray path length, which equals the distance between the source and the sensor k .

$\text{Ref}(t, r)$ is the reflection coefficient at the location of the sensor, which can be calculated from the direction cosine angle between the source and the observation station.

r_1, r_2, r_3 are three components of the direction vector between the source and the sensor k .

Notably, the number of sensors, k , needs to be larger than 6 to ensure that Eq. (3) becomes overdetermined to reach solutions after iteration. The iteration in this research is manipulated by the least square method, which is efficient in minimizing the discrepancy between recorded data and calculated results.

2.2 Decomposition of Moment Tensors

Moment tensor can be decomposed into three different components by Eq. (5) (Vavryčuk 2015): double couple (DC), isotropic components (ISO) and compensated linear vector dipole (CLVD), which are visualized in Fig. 1b. The DC component

(M_{DC}) is the off-diagonal element (M_{12}, M_{13}, M_{23}) to avoid rotation, which describes shear slip along a planar surface. The ISO component is the diagonal element (M_{11}, M_{22}, M_{33}) to describe volumetric change. A compensated linear vector dipole (M_{CLVD}) exists where the motion in one direction is compensated for by the motion in another. Even if the volumetric change is zero and meanwhile the summation of three diagonal elements is zero, the moment tensor decomposition still contains the CLVD component when one of the diagonal elements is compensated by others.

$$\mathbf{M} = M(C_{\text{ISO}}E_{\text{ISO}} + C_{\text{DC}}E_{\text{DC}} + C_{\text{CLVD}}E_{\text{CLVD}}), \quad (5)$$

where M is the norm of moment tensor \mathbf{M} ; E_{ISO} , E_{DC} , and E_{CLVD} are the base tensors for the ISO, DC and CLVD components, respectively. C_{ISO} , C_{DC} , and C_{CLVD} represent the corresponding percentage of these components.

The proportion of different components can be calculated by Eq. (6a, b, c) to quantitatively estimate different source mechanisms (Jost and Herrmann 1989).

$$C = \frac{\text{tr}(M)}{(\text{tr}(M) + \sum |m_i^*|)}, \quad (6a)$$

$$C_{DC} = \frac{m_3^*(1 - 2\varepsilon)}{|m_3^*(1 - 2\varepsilon)| + |2m_3^*\varepsilon|} (1 - C_{ISO}), \quad (6b)$$

$$C_{CLVD} = \frac{2m_3^*\varepsilon}{|m_3^*(1 - 2\varepsilon)| + |2m_3^*\varepsilon|} (1 - C_{ISO}), \quad (6c)$$

where $tr(M) = m_1 + m_2 + m_3$ is the trace of the moment tensor and m_i^* is the deviatoric eigenvalue ($m_i^* = m_i - tr(M)/3$, where m_i is the i -th eigenvalue). ε is the parameter for estimating the deviation of a seismic source from a pure double couple:

$$\varepsilon = -\frac{M_{|\min|}^*}{|M_{|\max|}^*|}, \quad (7)$$

where $M_{|\min|}^*$ and $M_{|\max|}^*$ are the minimum and maximum deviatoric eigenvalues among m_i^* in the absolute sense. With known percentage of different components, a crack induced by hydraulic fracturing can be characterized into shear, tensile or mixed mode, which will be discussed at length in Sect. 4.3.

In addition to the source type characterization, the moment tensor can also be decomposed to obtain the geometry of an induced crack, which is another important objective in this research. As aforementioned, a crack can be conceptualized as a small-scale fault. The conceptual fault can be denoted by two fault planes and a slip vector along the plane surface. The basic orientation parameters of a fault plane (strike, dip, and rake) can be derived from different components of a moment tensor (Tape and Tape 2012). The fault plane is characterized by \mathbf{n} , its normal vector, and its direction of motion given by \mathbf{s} , the slip vector on the fault plane. The slip vector, which always lies in the fault plane, is therefore perpendicular to the normal vector. It indicates the direction in which the hanging wall (upper side) moves against the footwall (lower side). Figure 2a defines the geometry of a fault using strike (φ), dip (δ), and rake (λ , also called slip angle). The unit normal vector \mathbf{n} has three directions in space (east \mathbf{n}_1 , north \mathbf{n}_2 , and down \mathbf{n}_3):

$$\mathbf{n} = \begin{bmatrix} n_1 \\ n_2 \\ n_3 \end{bmatrix} = \begin{bmatrix} -\sin\delta\sin\varphi \\ -\sin\delta\cos\varphi \\ \cos\delta \end{bmatrix} \quad (8)$$

A unit slip vector on the fault plane can also be defined by three basic orthogonal vectors:

$$\mathbf{s} = \begin{bmatrix} \cos\lambda\cos\varphi + \sin\lambda\cos\delta\sin\varphi \\ -\cos\lambda\sin\varphi + \sin\lambda\cos\delta\cos\varphi \\ \sin\lambda\sin\delta \end{bmatrix} \quad (9)$$

On the fault plane, different source mechanisms obtained from the moment tensor can also be displayed. A shear crack would only have a pure slip along the plane surface while a tensile crack would have the deformation along the normal direction of two fault planes but without any slippage. The mixed source mechanism would have both the slip and the normal deformation. The slippage and opening directions of a fault along with their radiation patterns given by Green's function in Eq. (4) are present in Fig. 2b and c, respectively. For a pure shear crack, the P-wave has two radiation directions with an angle of 45 degrees concerning both the normal and slip direction. Whereas for a tensile crack, P-wave has only one radiation direction along the fault normal.

3 Experimental Device and Procedure

3.1 Equipment of Laboratory Hydraulic Fracturing

Hydraulic fracturing experiments were carried out by the multi-physical rock testing platform (MRTP) shown in Fig. 3. The self-designed platform was developed through the integration of the servo loading frame, fluid injection unit and data recording system. It enables real-time measurement of permeability, P/S-wave velocity, and sample's deformation, along with continuous AE waveform recording under high pressure and high temperatures up to 200 °C.

The loading frame consists of a servo-controlled axial loading frame and a triaxial high-pressure loading cell. The axial loading frame boasts a maximum capability of 1500 kN. The triaxial high-pressure loading cell incorporates a pressure intensifier with a maximum capacity of 140 MPa used to supply thermal hydraulic oil and confining pressure. With a 175 mm internal diameter, the cell accommodates in-vessel measurements through electrical feed-through connectors installed at the cell base. The customized specimen platens are equipped with O-ring grooves to seal the specimen jacket and an upper spherical seat to minimize stress concentrations due to non-parallel specimen ends. Meanwhile, the platen functions as an injection line for gas and liquid, while also serving as a P/S-wave transmitter for wave velocity measurement.

The fluid injection unit includes pipelines and a high-pressure damping pump. Capable of delivering 2 litres of liquid at a constant rate from 1 ml/min to 130 ml/min, the injection rate can be adjusted to a smaller range easily via a hydraulic relief valve. Figure 3b and c demonstrates the sample configuration inside the loading vessel. The pipeline connects two ports on both upper and lower specimen platens. Flow meters, pressure transducers, and fluid connectors are provided at the cell base for easy connection with the computers for loading control and data recording.

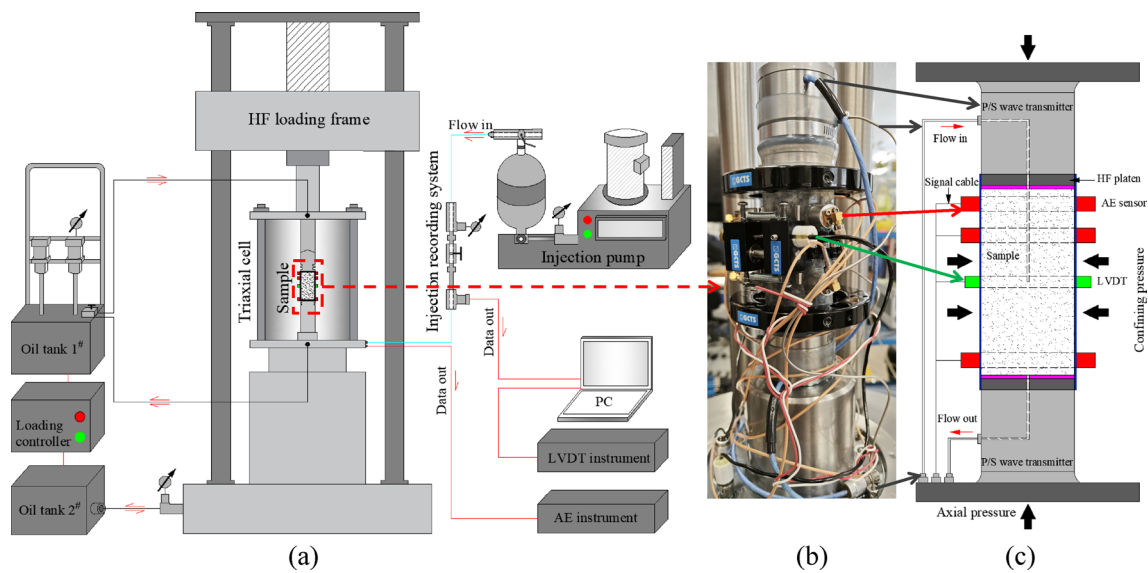


Fig. 3 Multi-physical rock testing platform (MRTP) for hydraulic fracturing: **a** Diagram of the triaxial hydraulic fracturing platform; **b** and **c** Sample configuration inside the loading cell

Table 1 Properties of Harcourt granite

Rock property	Value
UCS, MPa	91.01
Tensile strength, MPa	8.58
Young's modulus, GPa	22.02
Density, kg/m ³	2.79×10^3
Porosity, –	0.45%
P-velocity, m/s	4800
Poison's ratio, –	0.31
Fracture toughness (K_{Ic}), MPa·m ^{1/2}	1.11

To detect the internal failure behavior of test material inside the vessel, particularly the microcrack generation and propagation, AE monitoring and sample displacement measurement are adopted as a part of the data recording system. Figure 3b and c shows that one linear variable differential transformer (LVDT) is bound around the specimen to record the circumferential displacement and besides, eight AE sensors are affixed to the surface to collect AE signals generated during rock failure.

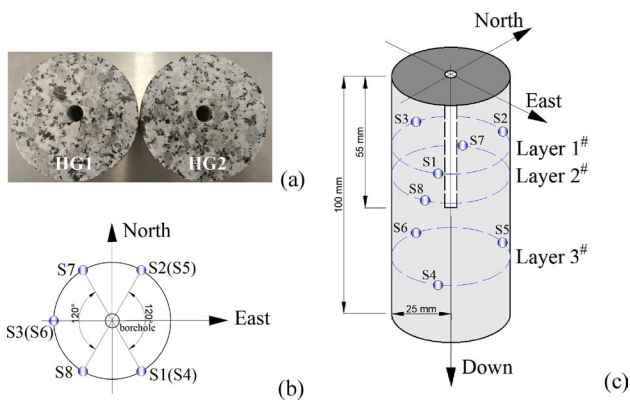
3.2 Sample Preparation and Test Procedure

Cubic rock blocks were quarried by a water jet cutter from a gray Harcourt granite (HG) field located in Melbourne, Victoria, Australia. The X-ray diffraction (XRD) test gives a composition table of 22.6% low-quartz, 59.9% feldspar mixed by plagioclase, microcline, and orthoclase; 8.6% clinocllore; and 8.9% illite. The core samples measuring

at 50 mm in diameter were drilled from a large block and trimmed to 100 mm length using a diamond blade saw, and then ground and polished to achieve a smooth and leveled surface. A P-wave ultrasonic velocity test was conducted on all samples to confirm homogeneity. The basic mechanical properties of the test materials, listed by Table 1, were measured following the ISRM test procedure to provide a reference for the principal stress set-up and serve as a basis for rock failure analysis. Seen in Fig. 12a in Appendix, the cylinders, equipped with strain gages, underwent loading at a rate of 0.5 MPa/s in the measurement of uniaxial compression strength (Bieniawski and Bernede 1979). The disk, featuring a notch, was fabricated in accordance with test instructions to assess the Mode I fracture toughness (Kuruppu et al. 2014). More details of tested samples along with the set-up can be referenced to Table 6 and Fig. 12 in Appendix. The injection borehole with a 55 mm length and 6 mm diameter was drilled along the axial direction from the centroid of the top surface to the middle of the sample. Epoxy was sprayed on the borehole wall and top surface of the sample to enhance the sealing effect. At the bottom of the borehole, a short distance (~10 mm) was left without epoxy to create an initial spot for fracturing. The injection parameter and the AE monitoring set-up are summarized in Table 2. The layout of the AE sensor array and the sample dimension are illustrated in Fig. 4b and c. To improve the spatial coverage over the sample, AE sensors in the same layer were spread at 120 degrees spacing around the sample. Table 5 in Appendix lists the sensor coordinates at different layers. All sensors underwent a pencil lead break test to ensure the coupling effect with the sample surface.

Table 2 Test set-up of hydraulic fracturing on Harcourt granite

Name	Value
<i>AE monitoring</i>	
AE recording threshold, dB	42
Sampling rate, SPS	2×10^6
Sensor operating frequency range, kHz	25–775
<i>Injection</i>	
σ_1/σ_3 ($=\sigma_2$), MPa	30/15
Injection rate, ml/min	10
Viscosity of injection water, Pa·s	10^{-3}


Fig. 4 a Granite specimen HG1 and HG2 and the layout of AE sensors; b Top view; c Oblique view

Two Harcourt granite samples, designated as HG1 and HG2, were tested as shown in Fig. 4a. Prior to fracturing, the injection pipe was filled with water to evacuate the air. Subsequently, the pipe was connected to the port of the hydraulic fracturing platen with 1–2 MPa pressure holding for 5 min to examine the sealing effectiveness of the entire system. After the holding pressure was released to zero, injection began at a constant flow rate of 10 ml/min and meanwhile all the recording system was initiated. Once the sample was broken, water would be released from the pipeline outlet and then the injection would be promptly ceased.

The AE system will continue recording for an additional 10 s after the injection ceases to capture all possible cracking signals. Prior to computations using the equations outlined in Sect. 2, the recorded waveforms need preprocessing. The electronic signals in voltage must be converted to waveforms in m/s or m. Subsequently, the time–frequency features of the calibrated waveforms will be analyzed to ensure they originate from rock cracking rather than environmental noise or other disturbances. Before being utilized in moment tensor calculation, AE events will be located, and meanwhile the travel distance of the radiated waveforms will be determined. The subsequent sections will elaborate on the detailed procedure and the algorithms necessary in moment tensor computation.

4 Results and Interpretation

4.1 Injection Measurements and Waveform Characterization

Direct recordings of injection pressure, AE count, and circumferential displacement from two samples are present in Fig. 13 in Appendix. Since HG1 and HG2 have close measurement results such as the injection duration, peak injection pressure and maximum AE counts, only sample HG1 will be discussed in detail in the following sections. As summarized in Table 3, sample HG1 experienced an injection of 720 s and was broken at 30.2 MPa generating 3.27×10^4 AE hits. A portion of data close to the peak value of AE count is extracted as shown in Fig. 5. All waveforms of 8 channels are stacked for clear cross-plotting with the injection pressure and displacement data.

Evidently, injection pressure, circular displacement, and waveform amplitude do not reach their peak values simultaneously. Instead, the waveform arrives at the highest AE energy of 6 V at 684.0 s shortly after the peak injection pressure occurring at 683.69 s. Afterwards, the maximum circular displacement appears at 684.66 s. When the injection pressure reaches its maximum, the circular deformation of the sample deviates from zero. The derivative of injection pressure with time (dP/dt) is depicted in the green line to estimate the decay rate, where positive dP/dt refers to a decrease in injection pressure. When the pressure reaches a maximum dP/dt at 683.9 s, displacement increases much faster than before and then the slope becomes gentler when the reduction in injection pressure slows down. Prior to its maximum, the displacement undergoes a brief period of decline, suggesting a potential fracture closure due to the supply shortage of injection fluid after its extensive diffusion into rock cracks. Notably, the maximum rate of changing pressure is happening very close to the time with the AE waveforms' peak magnitude and dramatic jump of circular displacement. The variation rather than the absolute value of injection pressure is a more apparent indicator to correlate the sample's deformation and AE responses.

The average amplitude of ambient noise becomes larger after the peak magnitude of AE waveforms at 684 s. This can be attributed to the fluid invasion following samples'

Table 3 Injection results of Harcourt granite

Name	Value
Injection duration, s	720
Maximum injection pressure, MPa	30.2
Maximum circular displacement, mm	2.0
Maximum AE count, –	3.27×10^4

Fig. 5 Hydraulic fracturing measurements during the failure process of Harcourt granite, from 682.0 s to 685.5 s

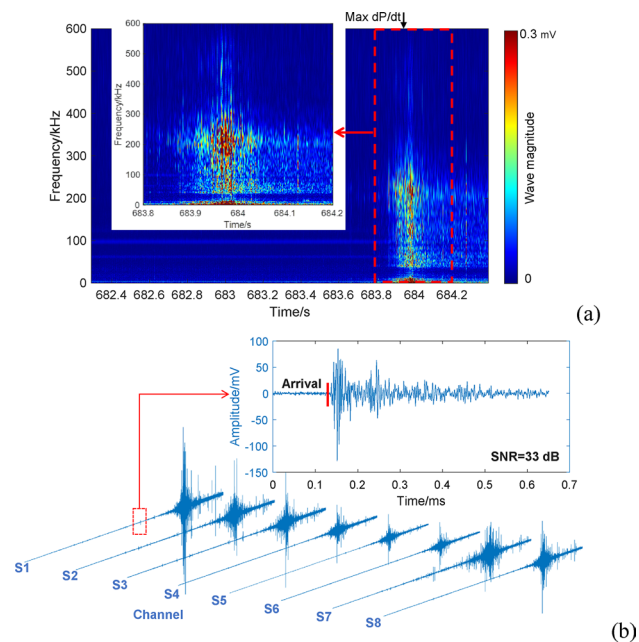
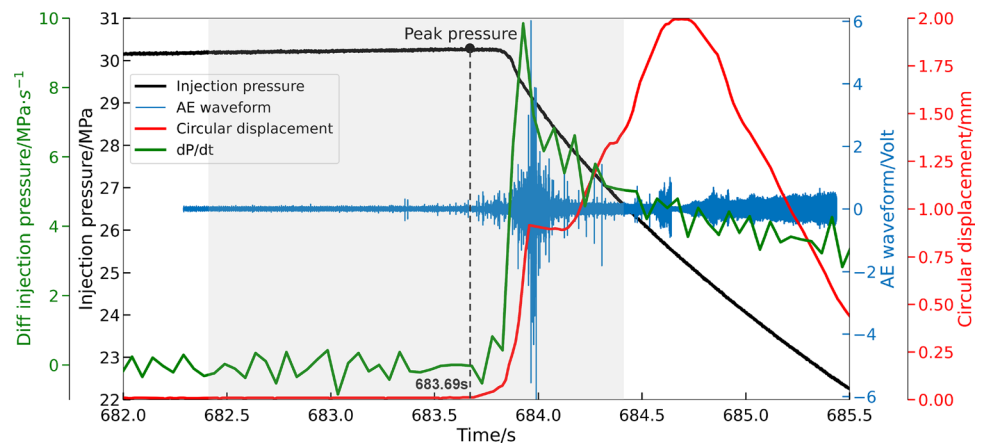


Fig. 6 **a** Time–frequency spectrum of waveforms; **b** Waveforms of 8 channels induced by rock failure under injection

breakage and unconsolidated velocity structure for P-wave traveling. Later at 684.48 s, waveforms with strong noise were recorded after a short period absence of effective waveforms. They were generated by disturbed fluid flow inside the fractured sample, as evidenced by continuous fluid pumping out through the cell outlet. Therefore, the period before 684.48 s, shaded by light gray in Fig. 5, is selected as a time window for subsequent detailed analysis.

Continuous wavelet transformation was carried out to confirm the effective waveforms generated by granite's failure. The time–frequency spectrum of the stacked waveforms from the shaded window in Fig. 5 is provided by Fig. 6a. The waveform has a broad range of frequencies extending up to 600 kHz when the sample is hydraulically fractured. The

dominant frequency is 200 kHz featured by the longest duration. Near the maximum derivative injection pressure (dP/dt), AE energy concentrates within the range of 30–300 kHz. The higher part of the frequency (400–600 kHz) has been classified as the AE events associated with fresh fractures inside the sample (Gehne et al. 2019), providing additional evidence of the rock's failure during the injection.

Waveforms in this window from all 8 sensor channels are plotted separately in Fig. 6b. Due to the excellent coupling between sensors and the sample, every channel has very clear and dense waveforms with strong magnitudes (ranging from –3.6 to 3.6 V). One of the less visible waveforms from sensor S1 is zoomed in to emphasize the high quality of signal recording. This waveform has a duration of 0.5 ms with a high signal-to-noise ratio (SNR = 33 dB), which is clear enough for accurate arrival time picking.

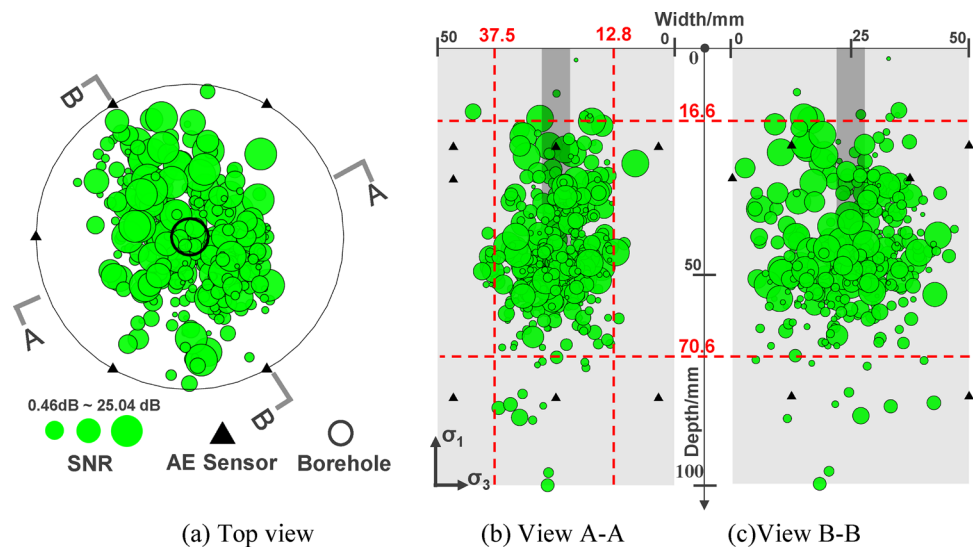
4.2 Fracture Mapping by Injection-Induced AE Events

The precise location of the induced hydraulic cracks premises reliable inversion of the fracture source mechanism. The collapse-grid search method under the homogeneous velocity model is employed here to locate seismic events. By reducing the iterative search volume of the best position (Li 2017), it becomes more effective than the conventional grid search method. The root mean square (RMS) error analysis algorithm is used to assess the quality of every location point.

$$E_{\text{RMS}} = V_p \sqrt{\frac{\sum_{i=1}^{i=N} T_i^2}{N}} \quad (10)$$

where T_i is the time residual between the measured traveling time from a waveform and the calculated traveling time obtained from the located source; N (> 5) is the number of arrivals or sensors chosen for locating; V_p is the P-wave velocity determined in Table 1. The spatial errors of all AE

Fig. 7 Spatial distribution of AE events



event locations are illustrated in Fig. 14 in Appendix. They have an average error of 2.66 mm suggesting reasonable location results. The majority of the AE events (87%) are reported within a 6 mm error. The void space in the borehole is a main contributor to location errors as it may bend the ray paths of radiated seismic waves inside the sample.

As seen in Fig. 7a, AE events are dispersed along both sides of the injection borehole but with a wider propagation along the B–B cut plane, forming an elongated belt of fracture clusters as observed by the top view. The sectional views of A–A and B–B in Fig. 7b and c reveal a clear failure plane vertically aligned with the maximum principal stress (σ_1). The cracking area is prominently concentrated in the top half of the sample, many of which are binding to the bottom of the injection borehole. Circle sizes are normalized in proportion to the average SNR of all employed sensors to depict the reliability of seismic localisation (Ren et al. 2021). Clearly observed from Fig. 7, most high-quality events are located around the borehole or along the main trace of the crack clusters.

To estimate fracturing area, four dashed red lines delineate the distribution of AE events. The width spans 24.7 mm from 12.8 to 37.5 mm away from the sample's side edge while the depth extends 54 mm ranging from 16.6 to 70.6 mm away from the top surface. Out of a total number of 377 AE events, more than 360 (> 90%) are located in this region encompassing those with high SNR values.

4.3 Evolution of Source Mechanisms Along with Fluid Injection

Utilizing the theories and methods described in Sect. 2.2, this section involves a comparison of source type solutions of each injection-induced crack. Computation results are scrutinized by condition numbers derived from eigenvalues of the generalized matrix of Green's function (Stump and

Johnson 1977). A smaller value corresponds to more reliable inversion results. The distribution of condition numbers from the moment tensor inversion of Harcourt granite is shown in Fig. 15 in Appendix. 84% of AE events have values less than 10, which provides evidence of satisfactory results. The percentage of the source type out of a moment tensor can be visualized by the Hudson plot (also known as the T–K plot) for easy comparison (Hudson et al. 1989; Jost and Herrmann 1989). The values on the T axis and K axis can be calculated through the following equations.

$$K = \frac{\frac{1}{3}tr(M) \times 100}{\left| \frac{1}{3}tr(M) \right| + \max(|m_1^*|, |m_3^*|)}, \quad (11a)$$

$$T = \frac{2m_2^*}{\max(|m_1^*|, |m_3^*|)}, \quad (11b)$$

where $tr(M) = m_1 + m_2 + m_3$ is the trace of moment tensor. m_1^* and m_3^* are deviatoric eigenvalues as shown in Eq. (6a, 6b, 6c). To ease the understanding of the calculation, two AE events defined as E1 and E2 are taken as examples and presented in Table 7 in Appendix. As displayed in Fig. 8a, most of the source types fall in the second and fourth quadrants, which means that all three components (ISO, DC, and CLVD) have the same signs of value. The cracks in these two quadrants have a dislocation source (shear-tensile) either for opening rupture (positive) or closure rupture (negative) (Vavryčuk 2015). For tensile cracks specifically, when $K > 0$, they exhibit outward displacement for opening. Whereas if $K < 0$, they have inward displacement for compression.

There are several criteria to define source types based on component percentage given by Eq. (6a, b, c). Two well-accepted methods are discussed here. The isotropic

Fig. 8 Source type analysis of hydraulic fracturing on Harcourt granite: **a** T–K plot; **b** Proportion of source type by moment tensor decomposition; **c** Proportion of seismic moment magnitude released in opening/closure cracks among all tensile events

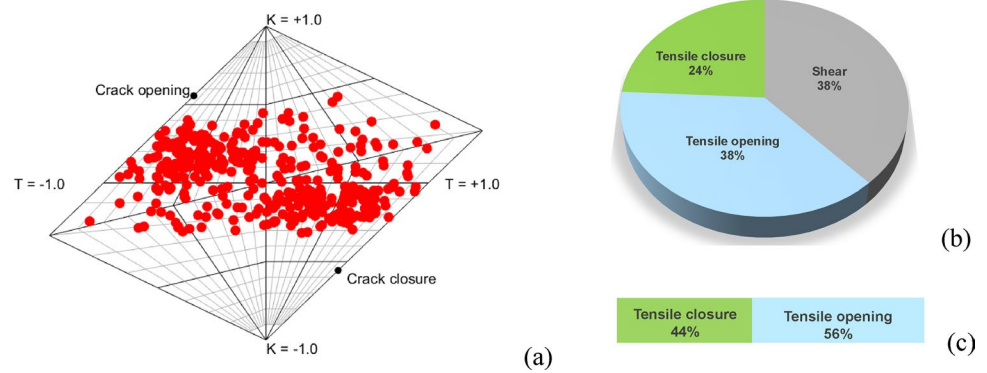
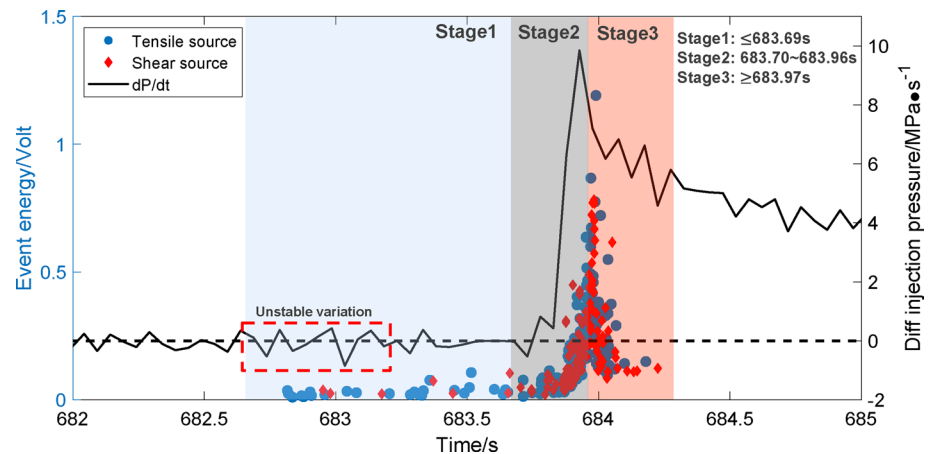


Fig. 9 Evolution of source mechanisms during rock's failure under injection



component dependent method assumes a crack to be tensile (including both opening and compression) if the absolute value of C_{ISO} is larger than 30. Otherwise, it will be classified as a shear crack (Feignier and Young 1992). Another popular method was proposed by Ohtsu (1991), which utilizes a double couple component (DC) to define three kinds of failure modes, namely tensile source, mixed source, and shear source if the C_{DC} value falls in the range of < 40 , $40-60$, and > 60 , respectively. To enhance the generalization, in this research, these two methods are integrated to define tensile and shear failure modes as follows: if the absolute C_{ISO} is larger than 30 or C_{DC} is smaller than 40, cracks can be classified as the tensile source type. Otherwise, the crack can be considered as a shear source crack. Since the mixed source cracks ($C_{DC} = 40 - 60$) are trivial in number in our research, they are included in the shear crack type.

Different source types are quantified in Fig. 8b and c, suggesting that a minority (38%) of all the AE events have a shear source mechanism, while the majority (62%) have the tensile source mechanism with more tensile opening events than (38%) tensile closure events (24%). Furthermore, the tensile opening accounts for 56% of the total moment magnitude released in all tensile source cracks. This dominance of the tensile source cracks, especially the tensile opening

component, is consistent with previous studies (Feignier and Young 1992; Fischer and Guest 2011).

To understand how these failure modes have evolved with time during injection, they are plotted in the time and energy domain in Fig. 9. The energy of every AE event is characterized by the average waveform amplitude in voltage from its eight channels. Based on the pressure peaks of the injection, the induced cracks are separated in the time axis to describe the fracture initiation and propagation inside the sample at different stages. As defined in Fig. 9, three stages shaded by different colors cover various peak values, including the peak injection pressure, maximum dP/dt and peak AE magnitude. At Stage 1 from 682.82 s to 683.69 s, the injection fluid pressure presents an unstable variation indicated by a larger differential value compared with the earlier time. Simultaneously, AE events with low amplitudes have already been induced even before the peak injection pressure. Although smaller in energy, the average SNR of waveforms at Stage 1 (SNR = 5.04) is larger than that at Stage 2 (SNR = 2.15) and Stage 3 (SNR = 2.33). It indicates that as the signal energy increases during the rock's breakage, the noise also becomes stronger due to the fluid intrusion.

Despite that the event with the largest energy is a tensile crack, the average amplitude of AE events listed in Table 4 suggests a different story. The shear cracks have stronger

Table 4 Comparison between tensile and shear events in three stages

Stage	Average magnitude, mV		Proportion	
	Tensile events	Shear events	Tensile events	Shear events
1	37.2	43.2	78.3%	21.7%
2	161.1	158.0	59.6%	40.4%
3	302.5	327.0	59.7%	40.3%

energy than the tensile cracks in Stage 1 and Stage 3, and the energy of these two kinds of failure is nearly the same in Stage 2. Overall, the shear cracks have a lower event number but possesses larger average AE event energy. Moreover, the tensile cracks constitute a dominant majority (78.3%) of all events at Stage 1, surpassing the overall proportion (62%) of the entire injection period. In the following stages, there is a substantial increase in AE events followed by a dramatic drop in fluid injection pressure. At the same time, more shear cracks with large magnitudes are induced, accounting for 40% of all events in these stages as seen in Table 4.

More obvious dominancy of tensile cracks at the early stage of rock failure was observed in previous tests on granitic materials and it was found to depend on the higher viscosity of injection fluid such as oil, instead of water (Butt et al. 2023b). However, our result suggests that the dominancy of tensile failure can also happen using water as the injection fluid, proving that the viscosity is not the only contributing factor. Two reasons may explain the observed difference. First, cubic samples with much larger side length (165 mm) were used in previous tests and this resulted in larger injection volume at a lower flow rate (1 ml/min). In this case, seismic waveforms may be much weaker in energy due to smaller input energy and larger attenuation. Second, shear cracks have a stronger average energy than tensile cracks during hydraulic fracturing. It is more likely for shear cracks to be recorded by AE sensors even with lower input energy. Therefore, in our research, a smaller sample ($\varnothing 50$ mm) and larger injection flow rate (10 ml/min) may induce stronger radiated energy and cause smaller attenuation, significantly increasing the possibility for tensile cracks to be captured.

The distribution of the AE events is displayed in Fig. 10 to compare changing failure source mechanisms in three stages. The color map describes the occurrence sequences of tensile cracks (marked by solid dots) and shear cracks (marked by diamonds) in each stage. The size of the marker is in positive proportion to the event magnitude in Volt. Although with lower energy and smaller amount than following stages, tensile cracks at Stage 1 still have a clear fracture pattern consistent with the overall trace of the cracking clusters, as seen from the top view in Fig. 10a. As represented by the smaller yellow and light green dots, the sparse distribution of events with much lower energy is recorded at the beginning during the unstable injection pressure variation. Afterwards from

683.5 to 683.69 s, the number of relatively stronger events represented by larger blue dots increases. Most of them are clustering near the borehole bottom, as emphasized by the dashed rectangle in Fig. 10a. Obviously, the initiation of hydraulic fractures occurs close to but before the presence of the peak injection pressure. Specifically, the occurrence of stronger cracks near the borehole indicates the dramatic decline of injection pressure and fluid losses.

In Stage 2, the number of AE events increases exponentially and the events are distributed along the orientation guided by the events triggered in Stage 1. From the side view in Fig. 10b (left), dark blue dots of large size reveal that most high-energy events show clustering behavior near the borehole bottom. There are a few strong shear events in the clusters but tensile cracks still make up the majority of the high-energy events. Subsequently, more high-energy events are induced in Stage 3 in Fig. 10c and extend along the trace present by Stage 2. Different from Stage 2, strong shear cracks in Stage 3 occupy more space in the sample which is evident in Fig. 9 and the side view in Fig. 10c. Although Table 4 indicates a nearly same proportion of shear cracks between Stage 2 and Stage 3, the dominant distribution of shear cracks is formed by high-energy events at Stage 3 later after many tensile cracks are induced near the borehole bottom. The obvious trace of shear cracks provokes an interesting discussion in the following section.

4.4 Correlation Between the Trace Orientation of Shear Cracks and Their Slippage

To comprehend the occurrence of AE events with the shear source mechanism in Harcourt granite, only those with the shear source type are visualized in Fig. 11a. The sizes of solid dots are proportionally normalized by the absolute percentage of double couple component (C_{DC}) in a moment tensor. According to the fault plane solution explained in Sect. 3.2 and Fig. 2a, slip vectors can be calculated from two inverted fault planes. Easily obtained by conducting trigonometric transformation after strike, dip, and rake, the slip azimuth and the slip plunge are more direct to demonstrate the movement of a single crack horizontally and vertically. As shown in Fig. 11a, the concentrated shear events are distributed near the borehole bottom and demonstrate a dominant trace across the shear band of the sample. From the polar map in Fig. 11b and the histogram in Fig. 11c, 72% of shear source cracks have slip plunges from 40 to 73 degrees. The trace of the shear crack cluster has a dip angle of 59 degrees regarding the horizontal direction. This number falls within the range of slip plunges and is quite close to their mean value (54 degrees). This identification highlights the effect of individual shear cracks on the overall trend of their distribution: The distribution trace angle of hydraulic fractures with the shear source mechanism would

Fig. 10 Spatial distribution of AE events during three different injection stages

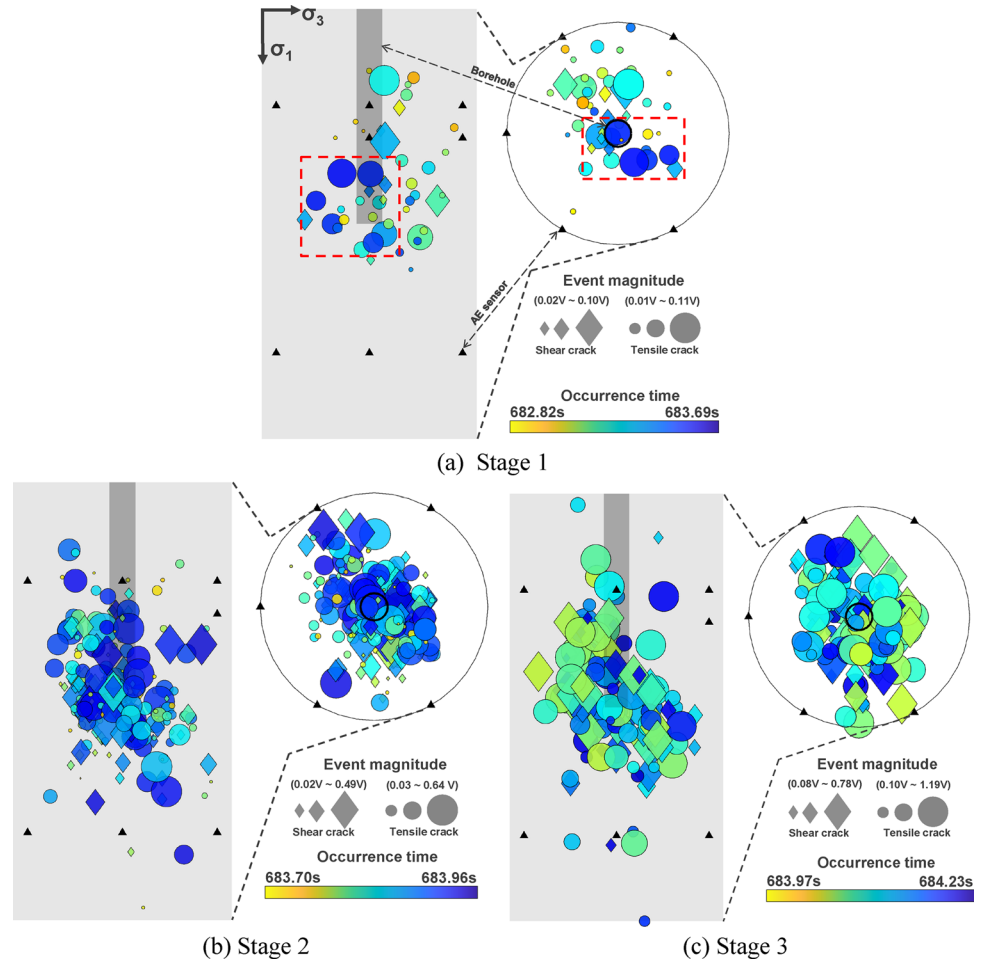
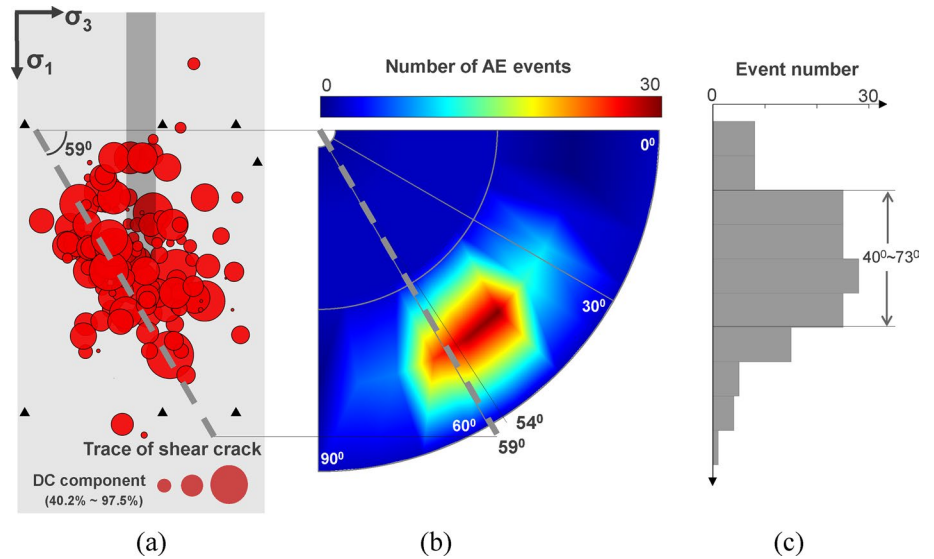


Fig. 11 **a** Distribution of shear cracks; **b** Plunge orientation distribution; **c** Histogram of event numbers with different slip plunges



follow the average slip plunges of individual shear cracks induced by the injection fluid. This correlation will contribute to enhancing channels of the fluid flow in hydraulic

fractures and predicting the potential slip orientation in injection-induced disaster prevention.

However, the observation that shearing cracks are induced by the pressurized fluid is inconsistent with the general

interpretation of tensile crack occurrence near the homogeneous injection borehole. Two factors may account for this observation. The first one is about the alteration from homogeneity to heterogeneity. In the early stages of the failure shown in Figs. 9 and 10 in Sect. 4.3, tensile cracks are initiated near the borehole earlier while shear cracks especially strong ones increase in number afterwards. These new tensile cracks may work as the pre-existing fractures and shear cracks are triggered by the immediate supply of pressurized fluid. Another reason is micro defects caused by the coarse grain size effect. In a microscope view, many crystalline rocks are not homogeneous, especially Harcourt granite composed of coarse size grains (> 1 mm) inside. The grain size plays a crucial role in the initiation and propagation of hydraulic fractures in brittle rocks. The larger difference in size between grains makes it more likely to generate defects like pre-existing fractures or microfractures, which will induce hydro shear type crack (Mode II crack) near fracture tips or grain boundaries (Zang et al. 2014; Zhuang and Zang 2021).

To further support our findings, results from the second test sample HG2 are present in Fig. 16 in the Appendix. Unlike HG1, HG2 exhibits two traces of shear cracks, but they have nearly the same trace dip angle of 57 degrees. The angle is quite close to the average slip plunge (60 degrees) of all shear cracks in Fig. 16b. Seen in Fig. 16c, 70% out of 106 shear cracks are slipping along the angles between 43 to 70 degrees. Results mirror those in HG1, providing additional validation of our analysis and result interpretation.

5 Conclusions

Laboratory hydraulic fracturing was conducted on Harcourt granite under triaxial loading. More than 370 effective AE events were picked to map water injection-induced fractures. Additionally, the source mechanism of these induced AE events was inverted by the P-wave first motion method to describe the evolving failure mechanisms spatially and temporally. Some important findings are summarized as follows:

- The failure of Harcourt granite under injection is completed in a short period of less than 1.5 s, yielding dense waveforms with high-energy and a broad-frequency band of 0–600 kHz. The injection pressure's variation rather than its absolute value becomes a more apparent indicator to correlate the AE energy and rock deformation. When the injection pressure reduces at the maximum rate, sample's deformation accelerates, and concurrently, waveforms reach their maximum magnitudes.
- Hydraulic fractures concentrate in the upper half of the sample and form an elongated belt of fracture clusters in the radial direction. Some cracks have been initiated before the peak injection fluid pressure with unstable

variation. Meanwhile, tensile cracks are induced at lower magnitudes but with greater proportion and higher signal-to-noise ratios than other periods. After peak injection pressure, the number and magnitudes of AE events increase tremendously. Most high-energy tensile cracks are distributed closely to the borehole bottom while most high-energy shear cracks are induced after the occurrence of massive tensile cracks.

- Shear cracks have larger average energy than tensile cracks. They have a dense concentration across the borehole bottom. The distribution orientation dip angle would follow the average angle of individual shear slips induced by the injection fluid. The existence of shear cracks and their influences are attributed to the heterogeneity caused by preliminary tensile cracks at the early failure stages and defects caused by the coarse grain effect due to the nature of granites.

Appendix

For appendix see Tables 5, 6 and 7 and Figs. 12, 13, 14, 15 and 16

Table 5 The coordinates of AE sensors

Layer	Sensor No	Sensor name	East, mm	North, mm	Down, mm
Layer 1 [#]	1	S1	12.5	-21.65	22.5
	2	S2	12.5	21.65	22.5
	3	S3	-25	0	22.5
Layer 3 [#]	4	S4	12.5	-21.65	72.5
	5	S5	12.5	21.65	72.5
	6	S6	-25	0	72.5
Layer 2 [#]	7	S7	-12.5	-21.65	30
	8	S8	-12.5	21.65	30

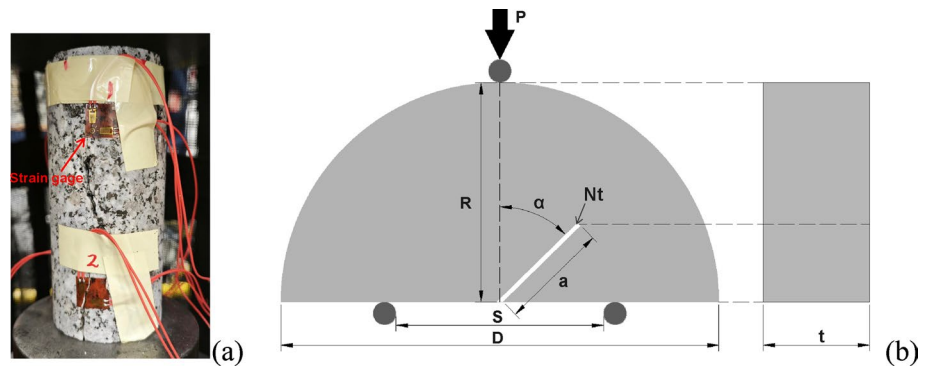
(The origin is at the top surface center of the sample)

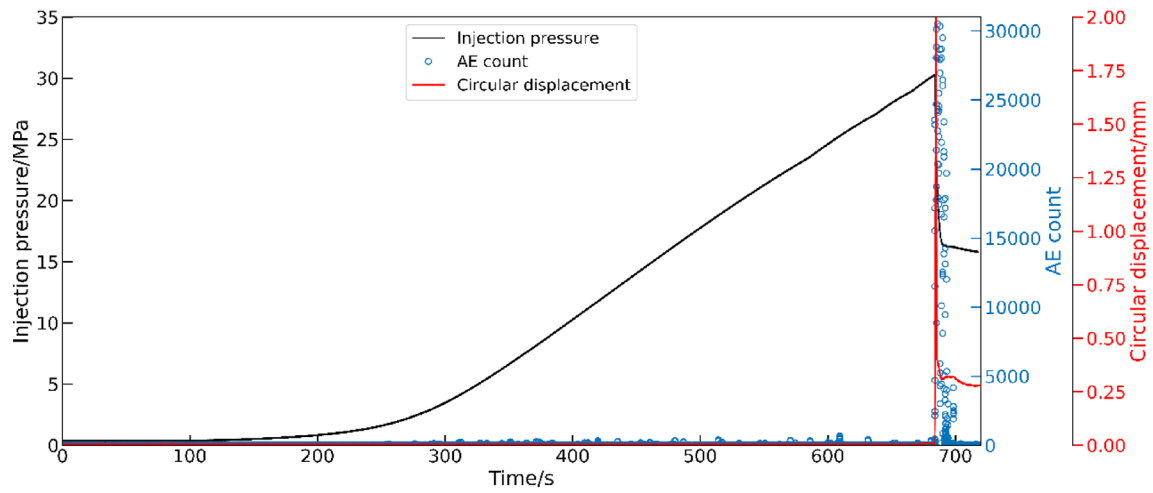
Table 6 Set-up of basic rock tests

Name	Symbol	Value
<i>UCS test</i>		
Length of cylinder, mm	<i>L</i>	100
Sample diameter, mm	<i>D</i>	50
<i>Brazilian test</i>		
Diameter of disk, mm	<i>D</i>	50
Height of disk, mm	<i>H</i>	25
<i>SCB test</i>		
Sample diameter, mm	<i>D</i>	95.4
Sample width, mm	<i>t</i>	45.95
Notch length, mm	<i>a</i>	24.10
Notch thickness, mm	<i>Nt</i>	1.5
Notch angle, degree	α	0
Span length, mm	<i>S</i>	50

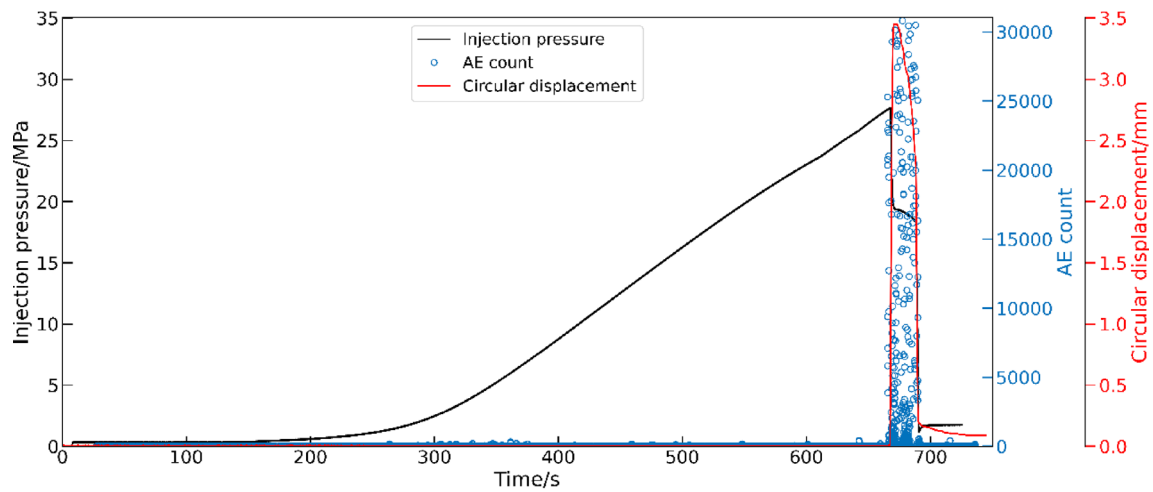
Table 7 Determination of source components from moment tensor

Event	E1	E2
Location (North,East,Down)	(10.253, -7.680, 53.120) mm	(11.059,2.381, 17.640) mm
Moment tensor	$\begin{bmatrix} 0.023 & 0.034 & -0.021 \\ 0.034 & 0.981 & -0.016 \\ -0.021 & -0.016 & -0.184 \end{bmatrix}$	$\begin{bmatrix} -0.248 & 0.110 & -0.242 \\ 0.110 & -0.029 & -0.225 \\ -0.242 & -0.225 & 0.834 \end{bmatrix}$
Eigenvalues	(-0.187, 0.024, 0.982)	(-0.315, -0.074, 0.946)
Deviatoric eigenvalues	(0.460, -0.249, 0.709)	(-0.501, -0.260, 0.760)
Component fraction (ISO/DC/CLVD)	36.61/18.79/44.60%	26.84/23.19/49.97%
T/K values	-0.704/0.278	-0.683/0.196

Fig. 12 **a** Set-up of uniaxial compression strength (UCS) test; **b** Set-up of semi-circular bend (SCB) test



(a) HG1



(b) HG2

Fig. 13 Evolution of AE count and circular displacement with fluid injection

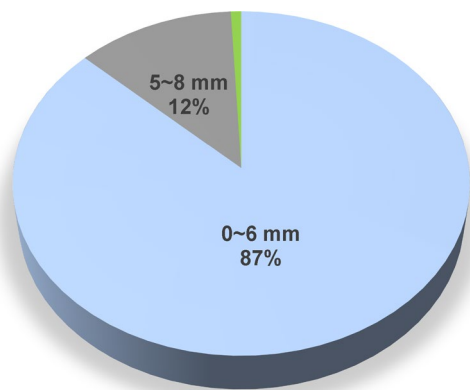


Fig. 14 Spatial errors' distribution of AE event location in HG1 (mean value = 2.66 mm)

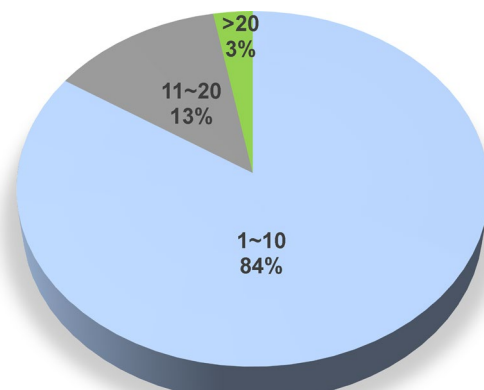
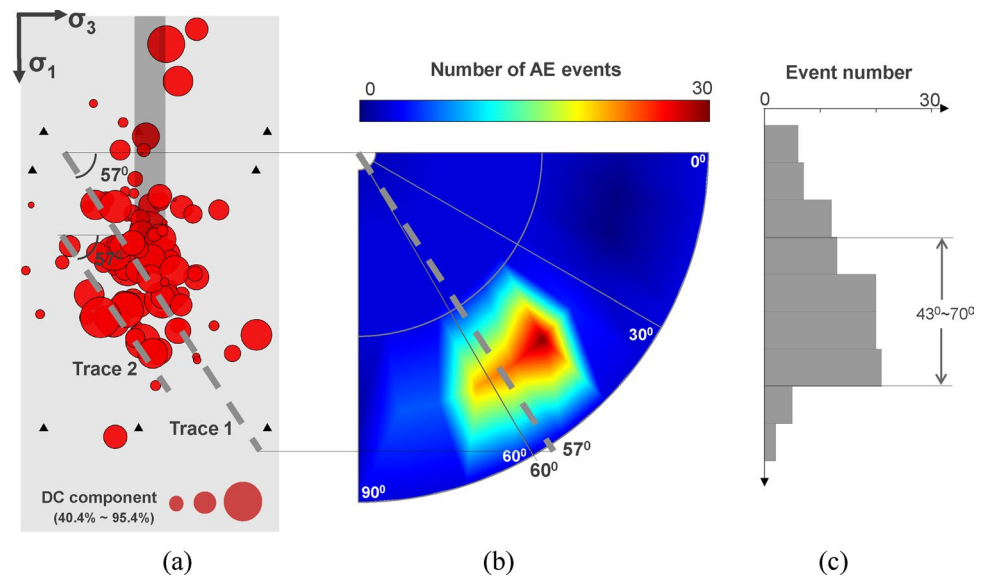


Fig. 15 Condition number distribution of HG1

Fig. 16 The trace of shear source events in HG2: **a** Distribution of shear type cracks; **b** Plunge orientation distribution of shear component in shear mechanism cracks; **c** Histogram of event number with different slip plunge



Acknowledgements The authors would like to thank Australian Research Council Linkage Program (LP200301404) for sponsoring their research work.

Funding Open Access funding enabled and organized by CAUL and its Member Institutions. Australian Research Council, LP200301404, Guangyao Si

Data availability Data will be made available on request.

Declarations

Conflict of interest The authors declare that they have no known competing financial interests or personal relationships that could have appeared to influence the work reported in this paper.

Open Access This article is licensed under a Creative Commons Attribution 4.0 International License, which permits use, sharing, adaptation, distribution and reproduction in any medium or format, as long as you give appropriate credit to the original author(s) and the source, provide a link to the Creative Commons licence, and indicate if changes were made. The images or other third party material in this article are included in the article's Creative Commons licence, unless indicated otherwise in a credit line to the material. If material is not included in the article's Creative Commons licence and your intended use is not permitted by statutory regulation or exceeds the permitted use, you will need to obtain permission directly from the copyright holder. To view a copy of this licence, visit <http://creativecommons.org/licenses/by/4.0/>.

References

- Aki K, Richards P (1980) Quantitative seismology. Sausalito, CA
- Bieniawski ZT, Bernede MJ (1979) Suggested methods for determining the uniaxial compressive strength and deformability of rock materials: part 1. Suggested method for determining deformability of rock materials in uniaxial compression. *Int J Rock Mech Min Sci Geomech Abstr.* [https://doi.org/10.1016/0148-9062\(79\)91451-7](https://doi.org/10.1016/0148-9062(79)91451-7)
- Butt A, Hedayat A, Moradian O (2023a) Laboratory investigation of hydraulic fracturing in granitic rocks using active and passive seismic monitoring. *Geophys J Int.* <https://doi.org/10.1093/gji/ggad162>
- Butt A, Hedayat A, Moradian O (2023b) Microseismic monitoring of laboratory hydraulic fracturing experiments in granitic rocks for different fracture propagation regimes. *Rock Mech Rock Eng.* <https://doi.org/10.1007/s00603-023-03669-6>
- De Natale G, Zollo A (1989) Earthquake focal mechanisms from inversion of first P and S wave motions. In: Cassinis R, Nolet G, Panza GF (eds) *Digital seismology and fine modeling of the lithosphere.* Ettore Majorana International Science Series. Springer, Boston, MA
- Economides MJ, Nolte KG (2000) *Reservoir stimulation.* John Wiley & Sons, New York
- Fairhurst C (1964) Measurement of in situ rock stresses with particular references to hydraulic fracturing. *Rock Mech Eng Geol* 2:129–214
- Feignier B, Young RP (1992) Moment tensor inversion of induced microseismic events: evidence of non-shear failures in the $-4 < M < -2$ moment magnitude range. *Geophys Res Lett* 19(14):1503–1506
- Fischer T, Guest A (2011) Shear and tensile earthquakes caused by fluid injection. *Geophys Res Lett.* <https://doi.org/10.1029/2010GL045447>
- Fu P, Settgest RR, Hao Y, Morris JP, Ryerson FJ (2017) The influence of hydraulic fracturing on carbon storage performance. *J Geophys Res Solid Earth.* <https://doi.org/10.1002/2017JB014942>
- Gehne S, Benson PM, Koor N, Dobson KJ, Enfield M, Barber A (2019) Seismo-mechanical response of anisotropic rocks under hydraulic fracture conditions: new experimental insights. *J Geophys Res Solid Earth.* <https://doi.org/10.1029/2019JB017342>
- Goodfellow SD, Nasser MHB, Young RP (2013) The influence of injection rate on hydraulic fracturing of tri-axially deformed westerly granite. Paper presented at the 47th U.S. Rock Mechanics/ Geomechanics Symposium, San Francisco, California
- Grigoli F, Cesca S, Priolo E et al (2017) Current challenges in monitoring, discrimination, and management of induced seismicity related to underground industrial activities: a European perspective. *Rev Geophys.* <https://doi.org/10.1002/2016RG000542>
- Hampton J, Gutierrez M, Matzar L, Hu D, Frash L (2018) Acoustic emission characterization of microcracking in laboratory-scale hydraulic fracturing tests. *J Rock Mech Geotech Eng* 10(5):805–817

- He Q, Suorinen FT, Oh J (2016) Review of hydraulic fracturing for preconditioning in cave mining. *Rock Mech Rock Eng.* <https://doi.org/10.1007/s00603-016-1075-0>
- Hudson JA, Pearce RG, Rogers RM (1989) Source type plot for inversion of the moment tensor. *J Geophys Res Solid Earth.* <https://doi.org/10.1029/JB094iB01p00765>
- Ishida T, Sasaki S, Matsunaga I, Chen Q, Mizuta Y (2000) Effect of grain size in granitic rocks on hydraulic fracturing mechanism. In: *Trends in Rock Mechanics, Geotechnical Special Publication*. 102: 128-139
- Jost ML, Herrmann RB (1989) A student's guide to and review of moment tensors. *Seismol Res Lett.* <https://doi.org/10.1785/gssrl.60.2.37>
- Kumari WGP, Ranjith PG, Perera MSA, Li X, Li LH, Chen BK, Isaka BLA, De Silva VRS (2018) Hydraulic fracturing under high temperature and pressure conditions with micro CT applications: geothermal energy from hot dry rocks. *Fuel.* <https://doi.org/10.1016/j.fuel.2018.05.040>
- Kuruppu MD, Obara Y, Ayatollahi MR et al (2014) ISRM-suggested method for determining the Mode I static fracture toughness using semi-circular bend specimen. *Rock Mech Rock Eng.* <https://doi.org/10.1007/s00603-013-0422-7>
- Li X, Si G, Oh J et al (2022) A pre-peak elastoplastic damage model of Gosford sandstone based on acoustic emission and ultrasonic wave measurement. *Rock Mech Rock Eng.* <https://doi.org/10.1007/s00603-022-02908-6>
- Li X, Lei X, Li Q (2023) Laboratory hydraulic fracturing in layered tight sandstones using acoustic emission monitoring. *Geoenergy Sci Eng.* <https://doi.org/10.1016/j.geoen.2023.211510>
- Li KL (2017) Location and relocation of seismic sources. Dissertation, Acta Universitatis Upsaliensis
- Lockner D (1993) The role of acoustic emission in the study of rock fracture. *Int J Rock Mech Min Sci Geomech Abstr* 30(7):883–899
- Ohtsu M (1991) Simplified moment tensor analysis and unified decomposition of acoustic emission source: application to in situ hydrofracturing tests. *J Geophys Res* 96(B4):6211e21
- Ohtsu M (1995) Acoustic emission theory for moment tensor analysis. *J Res Nondestruct Eval* 6:169–184
- Rathnaweera TD, Wu W, Ji Y, Gamage RP (2020) Understanding injection-induced seismicity in enhanced geothermal systems: from the coupled thermo-hydromechanical-chemical process to anthropogenic earthquake prediction. *Earth-Sci Rev* 205:103182
- Ren Y, Vavryčuk Ren WuS, Gao Y (2021) Accurate moment tensor inversion of acoustic emissions and its application to Brazilian splitting test. *Int J Rock Mech Min Sci.* <https://doi.org/10.1016/j.ijrmms.2021.104707>
- Schultz R, Skoumal RJ, Brudzinski MR, Eaton D, Baptie B, Ellsworth W (2020) Hydraulic fracturing-induced seismicity. *Rev Geophys.* <https://doi.org/10.1029/2019RG000695>
- Stanchits S, Surdi A, Gathogo P, Edelman E, Suarez-Rivera R (2014) Onset of hydraulic fracture initiation monitored by acoustic emission and volumetric deformation measurements. *Rock Mech Rock Eng.* <https://doi.org/10.1007/s00603-014-0584-y>
- Stein S, Wysession ME (2003) *An introduction to seismology.* Blackwell, Malden
- Stump BW, Johnson LR (1977) The determination of source properties by the linear inversion of seismograms. *Bull Seismol Soc Am* 67:1489–1502
- Tape W, Tape C (2012) A geometric setting for moment tensors. *Geophys J Int.* <https://doi.org/10.1111/j.1365-246X.2012.05491.x>
- Temizel C, Canbaz CH, Palabiyik Y et al (2022) A review of hydraulic fracturing and latest developments in unconventional reservoirs. Paper presented at the Offshore Technology Conference, Houston, Texas, USA. <https://doi.org/10.4043/31942-MS>
- Vavryčuk V (2015) Moment tensor decompositions revisited. *J Seismol.* <https://doi.org/10.1007/s10950-014-9463-y>
- Wang C, Si G, Zhang C et al (2021) A statistical method to assess the data integrity and reliability of seismic monitoring systems in underground mines. *Rock Mech Rock Eng.* <https://doi.org/10.1007/s00603-021-02597-7>
- Zhang X, Si G, Bai Q, Xiang Z, Li X, Oh J, Zhang Z (2023) Numerical simulation of hydraulic fracturing and associated seismicity in lab-scale coal samples: a new insight into the stress and aperture evolution. *Comput Geotech.* <https://doi.org/10.1016/j.compgeo.2023.105507>
- Zhuang L, Zang A (2021) Laboratory hydraulic fracturing experiments on crystalline rock for geothermal Purposes. *Earth-Sci Rev.* <https://doi.org/10.1016/j.earscirev.2021.103580>
- Zhuang L, Zang A, Jung S (2022) Grain-scale analysis of fracture paths from high-cycle hydraulic fatigue experiments in granites and sandstone. *Int J Rock Mech Min Sci.* <https://doi.org/10.1016/j.ijrmms.2022.105177>
- Zang A, Oye V, Jousset P, Deichmann N, Gritto R, McGarr A, Majer E, Bruhn D (2014) Analysis of induced seismicity in geothermal reservoirs – An overview. *Geothermics.* <https://doi.org/10.1016/j.geothermics.2014.06.005>

Publisher's Note Springer Nature remains neutral with regard to jurisdictional claims in published maps and institutional affiliations.